Eur. Phys. J. B **31**, 509–515 (2003)
DOI: 10.1140/epjb/e2003-00060-4

THE EUROPEAN PHYSICAL JOURNAL B

Evidence for a solid phase of dodecahedral C_{20}

Z. Iqbal[1,a], Y. Zhang[2], H. Grebel[2], S. Vijayalakshmi[2], A. Lahamer[3], G. Benedek[4], M. Bernasconi[4], J. Cariboni[4], I. Spagnolatti[4], R. Sharma[5], F.J. Owens[6], M.E. Kozlov[7], K.V. Rao[8], and M. Muhammed[8]

[1] Department of Chemistry, New Jersey Institute of Technology, Newark, New Jersey 07102, USA
[2] Department of Electrical and Computer Engineering, New Jersey Institute of Technology, Newark, New Jersey 07102, USA
[3] Department of Physics, Berea College, Berea, Kentucky 40404, USA
[4] Department of Materials Science and Istituto Nazionale per la Fisica della Materia, University of Milano-Bicocca, 20125 Milano, Italy
[5] Center for Solid State Science, Arizona State University, Tempe, Arizona 85287, USA
[6] Army Research and Engineering Center, Picatinny, New Jersey 07806, USA
[7] JDS Uniphase Corp, Eatontown, New Jersey 07724, USA
[8] Department of Materials Science and Engineering, Royal Institute of Technology, 10044 Stockholm, Sweden

Received 10 October 2002 / Received in final form 24 December 2002
Published online 6 March 2003 –

Abstract. Evidence is presented for the formation of a solid phase based on the smallest fullerene, C_{20}, in thin diamond-like carbon films deposited by ultraviolet laser ablation from diamond onto nickel substrates at room temperature in the presence of 10^{-4} torr of cyclohexane or benzene. Laser desorption mass spectrometry from the films shows the presence of C_{20}, C_{21} and C_{22} species, while micro-Raman spectroscopy and electron diffraction from selected particles together with first principle density-functional calculations, indicate a cubic solid with dodecahedral C_{20} cages as building blocks. Unlike solid C_{60} and fully protonated C_{20}, which are bound by van der Waals forces, the proposed structure is stabilized by linking of the C_{20} dodecahedra with bridging carbon atoms at interstitial tetrahedral sites to form a face-centered-cubic lattice with 22 carbon atoms per unit cell.

PACS. 61.48.+c Fullerenes and fullerene-related materials – 81.05.Tp Fullerenes and related materials – 61.50.Ah Theory of crystal structure, crystal symmetry; calculations and modeling – 81.07.Bc Nanocrystalline materials – 81.15.Fg Laser deposition

1 Introduction

Fullerenes smaller than C_{60} are of immense interest because they are likely to be precursors to a variety of novel carbon-based materials. Unlike the archetypal C_{60}, the smallest fullerene based on Euler's theorem, C_{20}, consists entirely of pentagons and is the carbon transliteration of Plato's dodecahedron [1]. C_{20} can be chemically synthesized in its fully hydrogenated form known as dodecahedrane, $C_{20}H_{20}$, where stability is achieved by saturation of the dangling bonds with hydrogen. On the other hand, it does not form spontaneously in carbon condensation or cluster annealing experiments [2,3], consistent with the expectation that only fullerenes with isolated pentagons separated by hexagons release strain and are therefore stable. This hypothesis has, however, been overturned by the recently reported formation of the bare small fullerenes, C_{20} and C_{36}, with adjacent pentagons. Prinzbach *et al.* [4] reported the surprising formation of dodecahedral C_{20} in the gas phase by dissociation of a $C_{20}HBr_{13}$ composition, while Koshio *et al.* [5], following the initial discovery of an unhydrogenated C_{36} solid [6], found that a $C_{36}H_4$ solid phase can be produced on nickel by laser ablation from a graphite target maintained at 1000 °C.

Here, we report the growth and characterization of a diamond-like carbon film with embedded crystallites, which we attribute to a C_{20} fullerene-based carbon solid. Laser ablation from a pure polycrystalline diamond instead of the usual graphite target used for the synthesis of fullerenes, is utilized. First principle density-functional calculations suggest a low energy structure comprised of C_{20} dodecahedra interconnected by two bridging carbon atoms per unit cell at the tetrahedral sites of a face-centered-cubic lattice. This structure is consistent with the Raman spectra and electron diffraction patterns from the particles, and laser-desorption mass spectra from the films. The relatively energetic laser ablation conditions used here have been previously shown to deposit stable thin films comprised of the hexagonal form of silicon [7] that is usually obtained only at high pressures.

[a] e-mail: zafar.iqbal@njit.edu

The paper is organized as follows: In Section 2 we present the experimental methods, while mass spectrometry, micro-Raman spectroscopy and transmission electron microscopy results on the deposited films, are presented and discussed in Section 3. The *ab initio* calculations on the properties of a theoretically conceived solid based on C_{20} clusters are reported and compared with the experimental data in Section 4, and conclusions are provided in Section 5.

2 Experimental methods

Pulsed laser ablation was performed with a 20-Watt KrF laser (Lamda Physik model EMG 102-MSC) emitting at a wavelength of 248 nm with 1.5 Watt of average power focused to a spot size of 100 μm^2 on a polycrystalline diamond target at ambient temperature. The polycrystalline diamond target used was 1.4 cm in diameter and produced by dynamic-pressure compaction of highly pure diamond powder [8]. X-ray diffraction showed that the target was composed of polycrystalline cubic diamond with less than 1% graphitic carbon. The target and a thin, high purity polycrystalline nickel substrate were mounted inside a stainless steel chamber with ultraviolet transmissive quartz windows, which was evacuated to a pressure of 10^{-6} torr. The substrate was placed at ambient temperature relatively close to the target at a distance of about 2.5 cm along the normal to the target surface. Laser ablation was carried out for 3 to 10 minutes under 10^{-4} torr pressure of cyclohexane or benzene to deposit films with a typical thickness of a few hundred nanometers. Films were also deposited in the presence of thiophene and in the absence of organics at 10^{-6} torr, and on quartz, copper, titanium and aluminum substrates.

Laser desorption time-of-flight mass spectral studies were conducted using a linear laser-desorption time-of-flight mass spectrometer from Comstock Inc and a nitrogen laser emitting at 337 nm that was highly attenuated to prevent extensive fragmentation [9]. The mass spectral data were obtained on as-deposited films that were removed from the substrates by immersion for less than 1 minute in dilute nitric acid, rinsed in deionized water and transferred to the sample head of the mass spectrometer.

Raman spectroscopic studies were performed using an Instruments SA/Dilor XY-micro-Raman spectrometer, a cooled charge-coupled-device (CCD) detection system and argon ion laser excitation at 514.5 nm with a power density of 1 to 5×10^3 Watt/cm^2 at the sample. The data discussed were obtained on as-deposited films scanned confocally at a spatial resolution of 1 to 2 μm.

Selected area electron diffraction and energy dispersive X-ray (EDX) analysis data were obtained with a 200 kV Philips CM 200 transmission electron microscope (TEM) linked to a CCD camera from Gatan. The specimens were prepared by floating the films off the substrates as described above, to a marker TEM grid on which a number of the locations of the new particles were identified by their Raman spectrum. Single crystal electron diffraction patterns were obtained from sufficiently thin crystallites at these locations, but like C_{36} and fullerenes in general, the crystallites suffered from slow electron beam damage at the incident beam energy of 200 kV. This precluded high-resolution lattice imaging and necessitated the use of lower beam intensities to obtain the electron diffraction patterns.

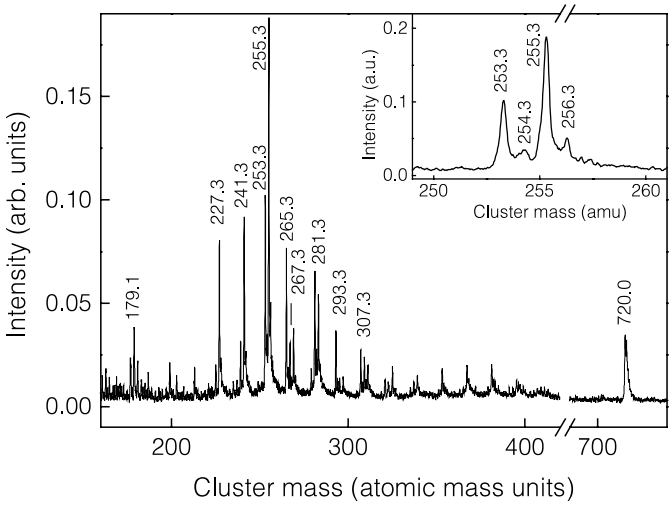

Fig. 1. Laser desorption time-of-flight mass spectrum in the 150 to 800 atomic mass range from a free standing film floated off the nickel substrate. Inset shows the detail around masses of 253 and 255 due to ^{13}C.

3 Results and discussion

3.1 Mass spectroscopy

A typical mass spectrum is displayed in Figure 1 showing lines around 720 amu (atomic mass units), which can be clearly assigned to the C_{60} fullerene, and a series of relatively intense lines at masses of 307, 293, 281, 265, 255, 253, 241, 227 and 179. The appearance of a line at 241 amu corresponding closely to the C_{20} mass suggests that the lines at 241 amu and above are associated with C_{20} in one of its isomeric forms – a fullerene cage, a bowl, or a ring [10]. The fullerene cage structure, although expected to be thermodynamically less stable, is likely to have formed because both the mass spectrum (Fig. 1) and Raman results (Sect. 3.2) indicate that C_{60} fullerenes are formed under our non-equilibrium synthesis conditions. The formation of fused ring polyacenic hydrocarbons are ruled out because of the absence of lines due to carbon-hydrogen stretching vibrations in the Raman spectra (Sect. 3.2) and the lack of intense visible fluorescence expected from the samples if polyacenes are present [11]. The observed mass spectrum can be attributed to three C_{20}-based series of anionic species that have the general formula: $C_{20}(NH)(NC)_n^-$, $C_{20}(NC)_nH^-$ and HC_{20}-C_n^-, where each species is composed of a C_{20} cluster attached to –$(NC)_n$, –C_n, –NH and –H. Functionalization by –NH and –H is likely to occur by interaction with nitric acid used to remove the film from the nickel substrate. Nitrogen is probably incorporated as–NC during film growth.

The lines at masses of 255, 281 and 307 are assigned to the $n = 0$, 1 and 2 members of $C_{20}(NH)(NC)_n^-$, whereas the lines at masses of 241, 267 and 293 are assigned to the $n = 0$, 1 and 2 members of $C_{20}(NC)_nH^-$. The lines at masses of 241, 253 and 265 are attributed to the $n = 0$, 1 and 2 members of the HC_{20}-C_n^- species. This indicates that C_{20}, C_{21} and C_{22} groupings are present in the solid. The clusters at lower masses grouped around 179 and 227 amu can be assigned to partially hydrogen-passivated C_{14} and C_{18} clusters, although the rationale for the specific appearance of these clusters in the desorption mass spectrum is unclear. It is worth noting that C_{19} represents the transition point between fullerene and non-fullerene clusters in accordance with Euler's theorem.

Bare or nearly bare carbon species are expected to show isotopic satellites with intensities corresponding to the 1.1% natural abundance of ^{13}C. These isotope peaks were indeed observed as evident from the data in Figure 1; for instance, the lines at 253 and 255 have satellites at masses of 254.2 and 256.3 with, as expected, 18% of the intensity of the primary line (inset, Fig. 1). Also, as expected, ^{13}C isotopic peaks are seen on the high mass side of the peak due to C_{60}. Films deposited using a graphite target under similar conditions did not show the mass spectral signatures of the C_{20}-based species discussed above and of C_{60}, indicating the importance of diamond as a precursor for the formation of fullerene solids under our experimental conditions.

3.2 Raman spectroscopy

The optical image of a typical film (deposited on a nickel substrate in the presence of a low pressure of benzene) shows light-gray regions (b in Fig. 2a inset) containing agglomerates of embedded dark particles (a in inset) that are 5 to 20 μm in diameter. The light-gray regions (b) displayed the Raman spectrum of amorphous carbon with a broad (linewidth of 150 cm^{-1} at half maximum intensity) graphitic (G) line at a frequency of 1530 cm^{-1} and a broad shoulder at 1300 cm^{-1} corresponding to the disordered (D) line. Some regions with dark particles were found, which displayed the Raman spectrum of photo-transformed C_{60} characterized by the strong pentagonal pinch mode at 1458 cm^{-1} [12] consistent with the observation of C_{60} in the laser desorption mass spectra discussed in Section 3.1 above. These particles could be thermally transformed to amorphous carbon by further increasing the laser power density. The dark particles, a, on the other hand were found to be relatively stable in the laser beam and showed a new Raman spectrum (Fig. 2). The assignment of the peaks to vibrations of the theoretically proposed C_{20}-based crystal is discussed in Section 4. Here we note that the strong line at 1175 cm^{-1} correlates with the strong Raman line at 1100 cm^{-1} observed in cluster-assembled amorphous C_{20} films [14]. Note also that the lines at 223 and 799 cm^{-1} fall in the range of the vibrational frequencies observed in the fine structure of the photoelectron spectra of C_{20} [4]. The line of medium intensity at 913 cm^{-1} can be assigned to a single bond

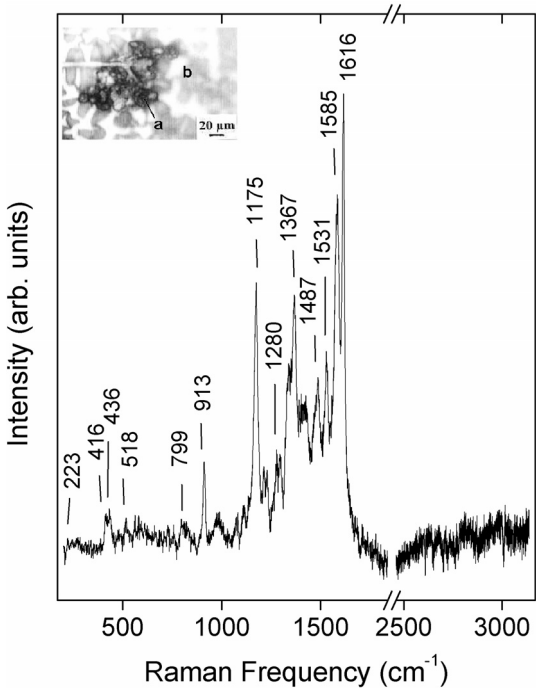

(a)

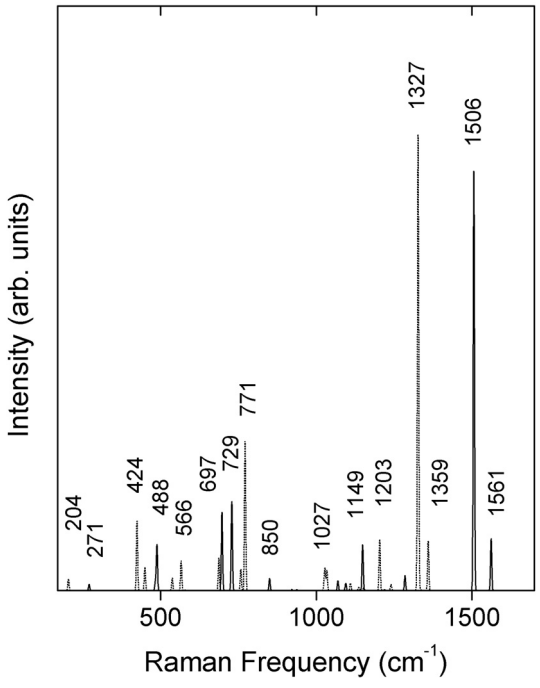

(b)

Fig. 2. (a) Raman spectrum of an as-deposited film at a spatial resolution of 2 μm from a dark particle in region a for which an optical image in the Raman microscope is shown in the inset. Region b displays the spectrum of an amorphous carbon as described in the text. (b) Schematic depiction of the theoretical Raman spectra of the C_{22} crystal (solid line) and of the C_{21} solid (dotted line).

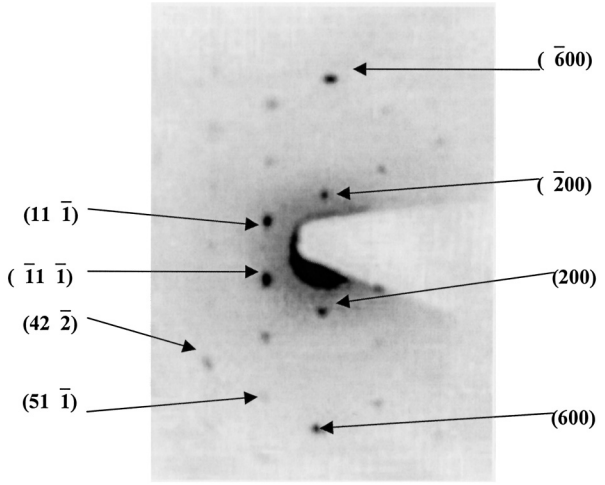

Fig. 3. Selected area electron diffraction pattern from a ⟨110⟩ oriented crystallite of the new phase. Some of the reflection indices are indicated in the figure. Note absences at positions of the (400) and ($\bar{4}$00) reflections which are expected to lie between the (600) and (200), and ($\bar{6}$00) and ($\bar{2}$00) reflections.

C-N stretching vibration consistent with presence of -NC groups indicated by the mass spectral data. Conversely, lines in the C-N triple bond stretching frequency region at 2200 cm^{-1} were not observed. No evidence for carbon-hydrogen stretching vibrations in the frequency region around 3000 cm^{-1} (Fig. 2) was found, indicating that the particles studied are not hydrocarbons. In addition, lines near 2200 cm^{-1} expected for carbon-carbon triple bonds in the chain, ring and bowl isomers of C_{20} [14], were absent. Raman measurements on a large number of films grown under various conditions showed that *the particles attributed to C_{20} and C_{60} were produced only when the films were grown under a low pressure of either cyclohexane or benzene, using polycrystalline diamond and nickel as target and substrate, respectively.* Films grown in vacuum or in low pressure of the sulfur-containing heterocyclic hydrocarbon, thiophene, showed the Raman spectrum of highly graphitized carbon embedded in the amorphous film.

3.3 Transmission electron microscopy

Crystallites that were sensitive to the electron beam were located in regions identified by micro-Raman spectroscopy on the TEM grids. These crystallites showed no impurity atoms by EDX and gave rise to diffraction spots. The electron diffraction pattern from a crystallite that could be aligned in the electron beam is displayed in Figure 3. The diffraction pattern is attributed to a ⟨110⟩ oriented face-centered-cubic (fcc) crystallite showing absences at the positions of the (400) and ($\bar{4}$00) reflections, and relatively high intensities for the ($\bar{1}1\bar{1}$), ($11\bar{1}$) and ($42\bar{2}$) reflections (Fig. 3). In addition, the (600) and ($\bar{6}$00) reflections as well as the ($42\bar{2}$) and ($51\bar{1}$) reflections (Fig. 3) appear to be split, possibly due to a combination of the instability of the particles in the electron beam and a small misalignment of the crystallite (110) face with respect to the beam. The latter also causes a small distortion of the diffraction pattern away from that of perfect fcc symmetry when calibrated against the ⟨110⟩ pattern from single crystal silicon.

The {200} and {111} *d*-spacings were measured to be 4.2 and 4.6 Å, respectively, corresponding to unit cell parameters of 8.4 and 8.0 Å. The 5% difference in unit cell parameters obtained from the *d*-spacings in two directions may be due to the presence of stress in the crystallites or caused by the misalignment discussed above. It is worth noting that the fcc lattice constants of 8.0 and 8.4 Å obtained are much smaller than the fcc unit cells of C_{60} and $C_{20}H_{20}$, which have lattice constants of 14.11 Å [15] and 10.61 Å [16] respectively.

4 Ab initio calculations

First principle calculations involving density-functional methods were carried out to determine a structure consistent with our experimental data. The method used involved: (a) norm-conserving pseudopotentials [17], (b) local density approximation (LDA), (c) plane wave expansion of Kohn-Sham orbitals up to 40 Rydberg cutoff, (d) special points in the integration of the irreducible Brillouin zone [18]. The Raman spectra were computed using *ab initio* phonons and static polarizability coefficients within linear response theory [19,20], which are valid for laser frequencies well below the band gap. The theoretical Raman intensities are not valid for resonant conditions.

A relatively low energy C_{20} fullerene-based fcc crystal structure was obtained with 4 Å diameter C_{20} cages (Fig. 4a) that are interlinked by two interstitial carbon atoms per unit cell at tetrahedral sites (Fig. 4b). A 4×4×4 Monkhorst-Pack (MP) mesh [18] within the irreducible Brillouin zone has been used in geometry optimizations. The crystal belongs to the $Fm\bar{3}$ space group and the unit cell contains one C_{22} formula unit. Only three atoms are independent, the other being obtained by symmetry operations. Their coordinates in units of the lattice constant are $A = (0.25, 0.25, 0.25)$, $B = (0.148, -0.148, 0.148)$, $C = (0.078, -0.217, 0.0)$ (Fig. 4b). Eight atoms out of twenty of the cage (atoms B) and the interstitial carbon atoms (A) are sp^3 hydridized. The other twelve atoms of the cage (C) are sp^2 hybridized forming C=C ethylenic bonds. There are three bond lengths in the crystal: the single sp^3-like B-C bond in the pentagonal ring (1.531 Å in length), the C=C ethylenic-like bond (1.346 Å in length) and the single sp^3-like bond between a cage (equivalent to B) and an interstitial atom (A) (1.517 Å in length). Although the properties of the isolated C_{20} cluster and the relative energies of the cage, bowl and ring isomers are very sensitive to the accuracy of the correlation functional (the ground state isomer is the cage, ring, or bowl within, respectively, LDA, gradient corrected functionals or quantum Monte Carlo calculation of the correlation energy [21]), we believe that the bonding properties of the C_{22} solid are closer to ordinary sp^2 and sp^3 solids than to

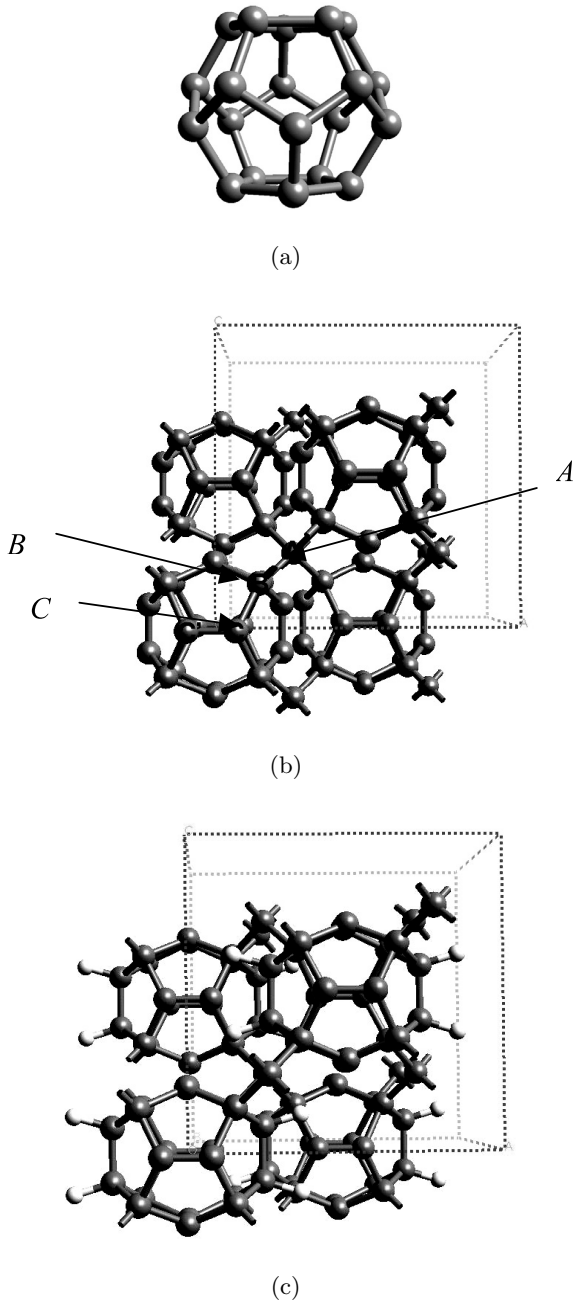

Fig. 4. Computer generated models for the structure of C_{20}-based crystal. (a) dodecahedral cluster C_{20}. (b) The face-centered-cubic structure of the C_{22} crystal. The conventional simple cubic unit cell with four formula units is shown. The crystal belongs to the Fm-3 space group and the coordinates of the three independent atoms in units of the lattice constant are $A = (0.25, 0.25, 0.25)$, $B = (0.148, -0.148, 0.148)$, $C = (0.078, -0.217, 0.0)$. The atoms C and C' and the other 10 of the cage equivalent by symmetry are linked by an ethylenic-like bond 1.346 Å long. (c) The corresponding structure of $C_{22}H_4$. In the structure shown in (c), hydrogenation up to 12 hydrogen atoms is achieved by linking sp^2 dimers with additional H atoms. Hydrogen positions are chosen in such a way as to minimize the electrostatic repulsion among H atoms belonging to different cages. The conventional, simple cubic cell with four formula units is indicated in each case.

the isolated cluster and therefore are more suitable to be accurately described by LDA.

Calculations of the equations of state yielded a cohesive energy of 0.63 eV/atom lower than that of diamond and a lattice constant of 8.61 Å. This value agrees within experimental error with the lattice constant of 8.4 Å from the observed {200} spacing. The calculated structure factor gives the following intensities for reflections from the $\langle 110 \rangle$ plane: (200) = 3.05, (400) = 0.25, (600) = 8.59, $(1, 1, \bar{1})$ = 15.00, $(4, 2, \bar{2})$ = 5.39, $(5, 1, \bar{1})$ = 8.79, indicating a near-absence at (400) and higher intensity at (600) and $(1, 1, \bar{1})$, which are in good agreement with the observed electron diffraction pattern (Fig. 3). The solid is an insulator with a slightly indirect XL band gap of 2.47 eV. Details on the electronic structure are given in reference [27]. Hydrogen can be incorporated into the structure as shown in Figure 4c, with only a small change in the lattice constant and a 0.27 eV/atom gain in cohesive energy with respect to the C_{22} crystal and molecular H_2. It may therefore be possible, as in the case of C_{36}, to prepare larger quantities of the hydrogenated analogue of the C_{22} solid under optimized hydrogen concentrations. The observed spectrum of masses generated by laser-induced fragmentation from our samples (Fig. 1) show a series of HC_{20}-C_n^- species corresponding to C_{20}-, C_{21}- and C_{22}-based fragments which are consistent with the proposed structure. The Raman line frequencies and intensities calculated for C_{22} using the theoretical unit cell of 8.61 Å, are reported in Figure 2b. At odds with the experimental data, only one intense peak is present in the theoretical spectrum; the line frequencies, however, are close to the experimental frequencies particularly when the lattice parameter is decreased to the experimental value of 8.4 Å. For example, the peak at 1560 cm^{-1} (Fig. 2), which is attributed to the stretching of the carbon-carbon double bonds in the C_{20} cages, shifts to 1627 cm^{-1} by decreasing the lattice parameter to the experimental value. The discrepancies with the intensities in the experimental spectrum may be due to resonant conditions in the experimental data since the spectrum was excited with photons close in energy to the direct band gap of 2.5 eV for the C_{22} structure and to the existence of nitrogen atoms in the structure indicated by both the mass spectral and Raman data discussed above. Moreover, partial disorder in the occupation of the tetrahedral sites in the real sample may be present. This is inferred from the calculation of the Raman spectrum of a C_{21} crystal (Fig. 2b), obtained by deleting one of the two interstitial atoms of C_{22}. The optimized C_{21} crystal is still fcc (space group F23, lattice constant 8.68 Å and positions of the four independent atoms in unit of the lattice constant (−0.2175, −0.0798, 0.0040), (−0.1482, 0.1482, 0.1482), (0.1362, −0.1362, −0.1362), (−0.25, 0.25, 0.25)), but is metallic with a cohesive energy 0.3 eV/atom lower than that of C_{22} due to the breaking of four covalent bonds per C_{20} cage. The Raman spectrum of the C_{21} solid (Fig. 2b) has been obtained from *ab initio* phonons and polarizability coefficients within the empirical Bond Polarizability Model [22] whose parameters for single and double bonds have been fitted to the *ab initio* calculated Raman

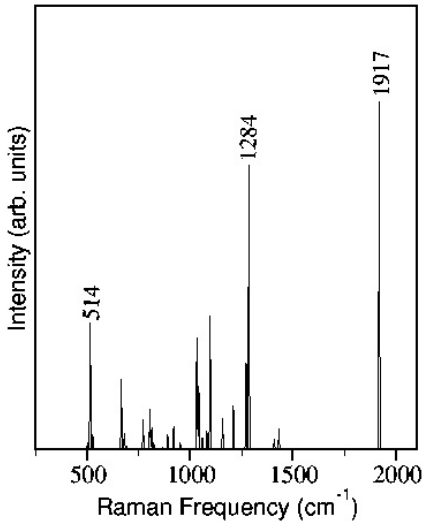

Fig. 5. Calculated Raman spectrum of the bco-C_{20} crystal (see text).

spectrum of C_{22}. The stretching modes of the C=C double bonds in C_{21} are shifted down by as much as 200 cm^{-1} with respect to C_{22} due to electron delocalization in the metallic C_{21} crystal (Fig. 2b). The superposition of the Raman spectra of C_{21} and C_{22} better match the experimental spectrum. This would indicate that the particles in our sample are likely to be a mixture of the C_{22} and C_{21} structures. Suitable fraction of the C_{21} phase and resonant effects in the polarizabilities may change the relative intensities of the theoretical peaks in Figure 2b to better reproduce the experimental intensities. We may also expect that other disordered configurations in the occupation of the tetrahedral sites (which would require larger simulation supercells), may produce an even richer Raman spectrum in the range 1100–1600 cm^{-1}, better matching the number and positions of the experimental peaks. Conversely, hydrogen incorporation (Fig. 4C) does not sizably shift the C-C stretching modes.

We have also considered another crystal structure based on C_{20} clusters [23] which turned out to be equivalent to the body-centered-orthorhombic C_{20} crystal (bco-C_{20}, Immm) recently proposed by Okada *et al.* [24]. We have fully optimized the structure by using a $4 \times 4 \times 4$ MP mesh. The calculated equilibrium lattice parameters are: $a = 6.142$ Å, $b = 5.934$ Å, $c = 7.580$ Å. The positions of the four independent atoms in unit of the lattice parameter a are (0.0, 0.3519, 0.1256), (0.1041, 0.0, −0.2309), (−0.3664, 0.1362, 0.0), (0.2054, 0.2084, 0.1989). These results are slightly different with respect to the calculations by Okada *et al.* [24], which reports a smaller orthorhombic distortion. This structure can be obtained from the C_{22} crystal by deleting the two interstitial carbon atoms, rotating the C_{20} cages by 45° and contracting the lattice parameters to the values of a, b, and c given above. The cohesive energy per atom of the bco-C_{20} phase is 32 meV higher than that of our C_{22} crystal. However, the geometry of bco-C_{20} is inconsistent with the TEM diffraction spots in Figure 3. We have also computed the Raman spectrum of bco-C_{20} (Fig. 5) within the same framework used for C_{21}, *i.e. ab initio* phonons and semiempirical polarizabilities. In the bco-C_{20} crystal there are two very short (1.278 Å) C=C double bonds per cage whose stretching mode gives rise to a strong Raman peak at 1920 cm^{-1} (Fig. 5) that is absent in the experimental Raman spectrum. Based on these results we can conclude that the bco-C_{20} crystal cannot represent the crystalline phase identified experimentally.

5 Conclusions

Our results provide evidence for the formation of a C_{20} fullerene based solid by ultraviolet laser ablation in the presence of cyclohexane or benzene from a diamond target placed relatively close to a polycrystalline nickel substrate at ambient temperature. Hydrogen from the hydrocarbon vapors in the ablation plume probably facilitates the formation of C_{20} dodecahedra from diamond by terminating the dangling bonds initially formed, followed by cross-linking with extra tetrahedral carbon atoms to form the proposed fcc structure C_{22} phase. As in the formation of C_{36}, nickel appears to play a critical catalytic role in the growth process, since particles with the new structure are not seen on substrates like quartz, copper, titanium and aluminum. The apparent formation of a C_{20} fullerene solid raises the possibility of using it, if it can be synthesized in larger quantities, to construct a template for the growth of metallic and superconducting single wall carbon nanotubes of the smallest diameter (4.2 Å) [25]. Another intriguing prospect is that a doped, more covalent solid based on the highly curved C_{20} may give rise to superconductivity at higher temperatures than in alkali-metal doped C_{60} [26,27].

Z. Iqbal acknowledges financial support from the Department of Army under contract DAAE30-02-C-1139. G. Benedek and M. Bernasconi acknowledge financial support from the INFM-project PRA CLASS and MURST-COFIN99 and PRIN01 under contract 2001021133. A. Lahamer would like to thank R.N. Compton at the University of Tennessee and Oak Ridge National Laboratory for discussions of the mass spectral data and for use of the LD-TOF mass spectrometer at the University of Tennessee, and the Undergraduate Research and Creative Projects program at Berea College for financial support. M. Muhammed and K.V. Rao acknowledge support from the Swedish funding agency NUTEK.

References

1. E. Heilbronner, J.D. Dunitz, *Reflections on Symmetry* (VCH, Weinheim, 1993)
2. G. Von Helden *et al.*, Chem. Phys. Lett. **144**, 431 (1988)
3. G. Von Helden, N.G. Gotts, M.T. Bowers, Nature **363**, 60 (1993)
4. H. Prinzbach *et al.*, Nature **407**, 60 (2000)
5. A. Koshio, M. Inakuma, T. Sugai, H. Shinohara, J. Am. Chem. Soc. **122**, 398 (2000)

6. C. Piskoti, J. Yarger, A. Zettl, Nature **393**, 771 (1998)
7. Y. Zhang, Z. Iqbal, S. Vijayalakshmi, H. Grebel, Appl. Phys. Lett. **75**, 2758 (1999)
8. V.S. Joshi, H.A. Grebe, N.N. Thadhani, Z. Iqbal, AIP Conference Proc. **309**, 1251 (1993)
9. R. Hettich, A. Lahamer, L. Zhou, R. Compton, Int. J. Mass Spectrometry **182/183**, 335 (1999)
10. M.F. Jarrold, Nature **407**, 26 (2000)
11. R.M. Hochstrasser, C.A. Nyi, J. Chem. Phys. **72**, 2591 (1980)
12. P.C. Eklund, P. Zhou, K-A. Wang, G. Dresselhaus, M.S. Dresselhaus, J. Phys. Chem. Solids **53**, 1391 (1992)
13. V. Paillard, Europhys. Lett. **54**, 194 (2001)
14. K. Raghavachari *et al.*, Chem. Phys. Lett. **214**, 357 (1993)
15. J.E. Fischer, P.A. Heiney, J. Phys. Chem. Solids **54**, 1725 (1993)
16. J.C. Gallucci, C.W. Doecke, L.A. Paquette, J. Am. Chem. Soc. **108**, 1344 (1986)
17. N. Troullier, J.L. Martins, Phys. Rev. B **43**, 1993 (1991)
18. H.J. Monkhorst, J.D. Pack, Phys. Rev. B **13**, 5188 (1976)
19. S. Baroni, S. de Gironcoli, A. Dal Corso, P. Giannozzi, Rev. Mod. Phys. **73**, 515 (2001)
20. We used the code CPMD version 3.0 written by J. Hutter *et al.* (Max Planck Institute for Solid State Physics and IBM Research Laboratory), and codes PWSCF and PHONONS written by S. Baroni *et al.*
21. G. Galli *et al.*, Phys. Rev. B **57**, 1860 (1998)
22. D.W. Snoke, M. Cardona, S. Sanguinetti, G. Benedek, Phys. Rev. B **53**, 12641 (1996)
23. A. Mussi, undergraduate thesis, Department of Physics, University of Milano (2001)
24. S. Okada *et al.*, Phys. Rev. B **64**, 245405 (2002)
25. Z.K. Tang *et al.*, Science **292**, 2462 (2001)
26. M. Schlüter, M. Lannoo, M. Needels, G.A. Baraff, D. Tomanek, J. Phys. Chem. Solids **53**, 1473 (1992)
27. I. Spagnolatti, M. Bernasconi, G. Benedek, Europhys. Lett. **59**, 572 (2002)